Additive Manufacturing Letters 3 (2022) 100097

Contents lists available at ScienceDirect

Additive Manufacturing Letters

journal homepage: www.elsevier.com/locate/addlet

Laser powder directed energy deposition (LP-DED) NASA HR-1 alloy: Laser power and heat treatment effects on microstructure and mechanical properties

Arash Soltani-Tehrani[a,b], Poshou Chen[c], Colton Katsarelis[c], Paul Gradl[c], Shuai Shao[a,b], Nima Shamsaei[a,b,*]

[a] National Center for Additive Manufacturing Excellence (NCAME), Auburn University, Auburn, AL 36849, United States
[b] Department of Mechanical Engineering, Auburn University, Auburn, AL 36849, United States
[c] NASA Marshall Space Flight Center, Huntsville, AL 35812, United States

ARTICLE INFO

Keywords:
Additive manufacturing
Laser power
Laser spot size
NASA HR-1
Iron-based superalloys

ABSTRACT

This study investigated the microstructure and tensile properties of the NASA HR-1 (Fe-Ni-Cr) alloy using the laser powder directed energy deposition (LP-DED) process. Laser power and spot size were varied for deposition, and it was noted that low laser power could result in higher cooling rates and finer microstructure. The melt pool depth and width and the defect content increased with the increase in laser power. Out of several laser power (i.e., 350, 750, 1070, 2000, and 2620 W), the samples deposited using 750 W demonstrated the highest material density. In addition, the effects of heat treatment on the microstructure and tensile properties were investigated. It was found that a heat treatment schedule consisting of stress relief, homogenization, solution treatment, and aging could thoroughly homogenize the microstructure (i.e., remove the as-solidified dendritic microstructure), result in relatively uniform, equiaxed grains, and increase the material hardness. Importantly, this heat treatment schedule efficiently reduced titanium segregation, preventing the formation of deleterious needle-shaped η (Ni_3Ti) precipitates in NASA HR-1, known to be detrimental to mechanical properties and resulted in almost comparable tensile properties with varying laser power.

Introduction

NASA HR-1 is a Fe-Ni based γ' strengthened superalloy alloyed with Co, Cr, Mo, W, Ti, Al, and V designed for high strength, weldability, and high-pressure H_2 environments [1]. This material was developed by altering the chemical composition of the A286 and JBK-75 alloys to improve strength and ductility for components such as liquid rocket engines' channel-cooled nozzles [1,2]. In the wrought form, compared to A286 and JBK-75, NASA HR-1 has superior thermal conductivity, fatigue resistance, yield strength, elongation to failure, and higher resistance to heat-affected-zone cracking during solidification, as well as oxidation, corrosion, and hydrogen environment embrittlement (HEE) resistance [1,3–5]. The chemistry modifications included the increase of Ni and Mo to diminish solidification cracks, maintaining Cr and V to provide sufficient resistance to corrosion/oxidation and notch effects, and the addition of W to further solution-harden the material and impede the formation of needle-shaped Ti-rich η-phase (Ni_3Ti) at or near the grain boundaries (which is detrimental to ductility). The Ti and Al were also increased to enhance the volume fraction of γ' ($Ni_3(Al,Ti)$) spherical precipitates [1,3].

NASA HR-1 was traditionally processed using vacuum induction melting (VIM) and vacuum arc remelting (VAR), followed by hot and cold rolling [3]. The NASA HR-1 alloy was adopted to additive manufacturing (AM) processes, such as laser powder directed energy deposition (LP-DED), due to the feasibility of rapidly manufacturing thin-wall and/or geometrically complex components at a reduced cost and lead time compared to traditional methods [2]. For LP-DED to strike a balance between build rate and geometric accuracy for a given component—i.e., a smaller melt pool offers better geometric accuracy but lower build rates and vice versa – the melt pool width can be adjusted

Abbreviations: AM, additive manufacturing/additively manufactured; EBSD, electron backscatter diffraction; ECCI, electron channeling contrast imaging; EDS, energy dispersive X-ray spectroscopy; FC, furnace cooling; HEE, hydrogen environment embrittlement; HT, heat treatment; HZ, homogenization; LP-DED, laser powder directed energy deposition; L-PBF, laser powder bed fusion; LAGB, low angle grain boundary; NHT, non-heat-treated; ST, solution treatment; SEM, scanning electron microscope/microscopy; SR, stress relief; UTS, ultimate tensile strength; WQ, water quench; YS, yield strength.

* Corresponding author at: Department of Mechanical Engineering, Auburn University, Auburn, AL 36849, United States.
E-mail address: shamsaei@auburn.edu (N. Shamsaei).

https://doi.org/10.1016/j.addlet.2022.100097
Received 2 September 2022; Received in revised form 18 October 2022; Accepted 19 October 2022

Nomenclature

Σ3	annealing twin boundary
ξ	grain zie

by controlling the laser spot size and power [1,2,6,7]. The adjustment is typically made simultaneously to both parameters. However, significant changes in melt pool size and geometry can cause significant changes in the thermal history experienced by the LP-DED parts, which can inevitably influence their defect-/micro-structure, and, thus, mechanical properties [8,9]. It is, therefore, essential to understand such influence to aid the design and fabrication of LP-DED parts with tailored surface conditions, defect-/micro-structure, and properties [1].

In addition, the high cooling rates in the LP-DED process can result in the formation of highly texturized and dendritic microstructure (with the dendrites oriented perpendicular to the melt pool boundaries) and volumetric defects potentially resulting in anisotropic material behavior as well as insufficient ductility [10,11], respectively. While the defects are generally difficult to remove via post-processing, the as-solidified dendritic microstructure can be removed by heat treatment (HT). However, a detailed understanding of the influence of HT on the microstructure of NASA HR-1 is presently lacking in the literature. Thus, this work investigates the effects of HT comprising several steps, including stress relief, homogenization, solution treatment, and aging, on the microstructure, hardness, and tensile properties of LP-DED NASA HR-1 parts deposited with different laser power (i.e., 350, 750, 1070, 2000, and 2620 W) to select the most desirable HT schedule. Following the Introduction, the Methodology, Experimental Results and Discussion, and Conclusions will be presented.

Methodology

Rotary-atomized NASA HR-1 powder (45–105 μm) from Homogenized Metals Inc (HMI) was employed to deposit bars and blocks via a RPM Innovations (RPMI) 557 LP-DED machine. The thickness (17 mm) of the bars and blocks were kept identical to maintain direct comparisons across the various spot sizes. The powder particle morphology and chemical composition were obtained via scanning electron microscopy (SEM) and energy-dispersive X-ray spectroscopy (EDS), respectively, and reported in Fig. 1. Hereon, the parts will be referred to by the laser power used for deposition (i.e., 350, 750, 1070, 2000, and 2620 W). A schematic of the LP-DED process using a coaxial laser-powder system is illustrated in Fig. 2(a). The resulting bars and blocks are shown in Fig. 2(b) and Fig. 2(c), respectively. Full details of process parameters are also provided in Fig. 2(d).

After deposition, parts were removed from the substrate using a bandsaw, and selected bars and blocks were transversely cut into multiple pieces for HT study, as illustrated with gray shades in Fig. 2(a). All the acquired sections were again cut along the longitudinal plane to measure hardness and investigate the microstructure on the longitudinal plane (along the building direction (BD)). Samples were analyzed in the NHT condition and at various stages of the HT. The HT schedule consisted of stress relief (SR), homogenization (HZ), solution treatment (ST), and two-step aging. The complete HT schedule is detailed in Table 1 and Fig. 3.

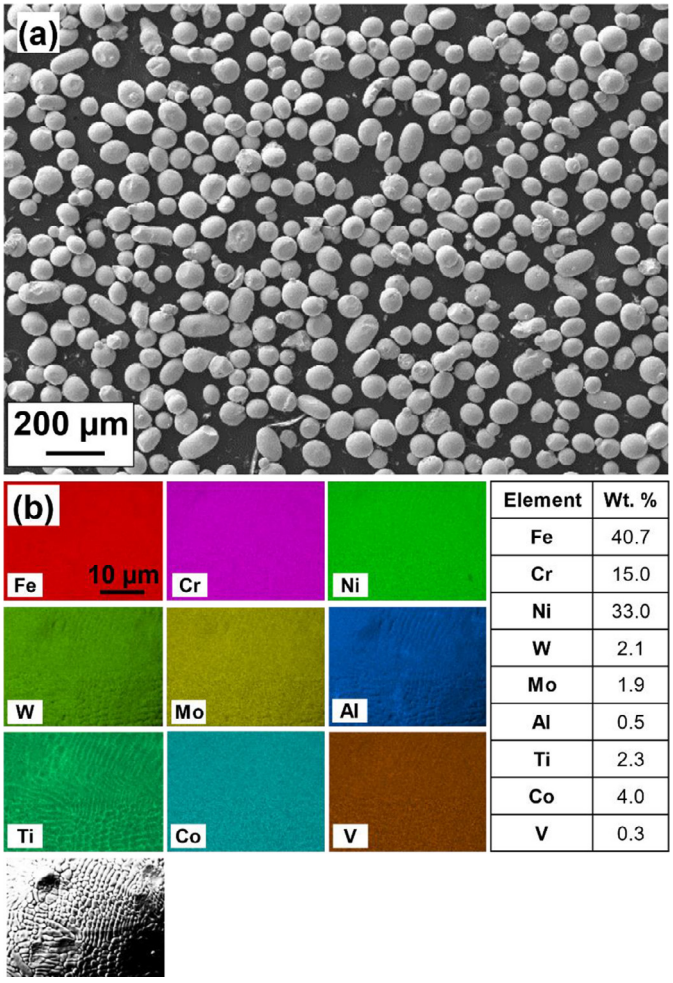

Element	Wt. %
Fe	40.7
Cr	15.0
Ni	33.0
W	2.1
Mo	1.9
Al	0.5
Ti	2.3
Co	4.0
V	0.3

Fig. 1. (a) NASA HR-1 powder particle morphology obtained via SEM, and (b) chemical composition acquired using EDS from a single particle.

After HT, samples were examined via electron backscatter diffraction (EBSD), EDS, and electron channeling contrast imaging (ECCI) to observe grain morphology and detect any elemental segregation. Rockwell B hardness (HRB) tests were conducted using LECO LCR-500 (at least three indentations per condition) according to the ASTM E2546 standard [12]. Each HT step will be hereafter referred to as its temperature and duration. For example, the SR1065/1.5 implies stress relief at 1065 °C for 1.5 h.

In the NHT condition, samples were etched using the Glyceregia reagent [13] along the BD to reveal the melt pool boundaries. Melt pool depth, overlap depth, and width were measured using a Keyence VHX-6000 digital optical microscope according to NASA MSFC 3717 [14]. Defect analysis on NHT samples fabricated with different laser power was based on optical microscopy performed on polished cross sections, which was a popular technique among AM practitioners due to its cost-effectiveness despite the increasing popularity of X-ray computed tomography. After selecting the proper HT, various round bars

Table 1
Heat treatment schedule for the LP-DED NASA HR-1 parts.

Heat Treatment	Temperature (°C)/Duration (Hours)	Quenching
Stress Relief (SR)	980/1.5, 1065/1.5, or 1065/3 [4]	Furnace cooled (FC)
Homogenization (HZ)	1165/3, 1165/6, or 1165/12	FC
Solution Treatment (ST)	980/1, 1065/1, or 1065/3	Argon quench (AQ)
Two-Step Aging (Aged)	690/16 and 621/16	FC

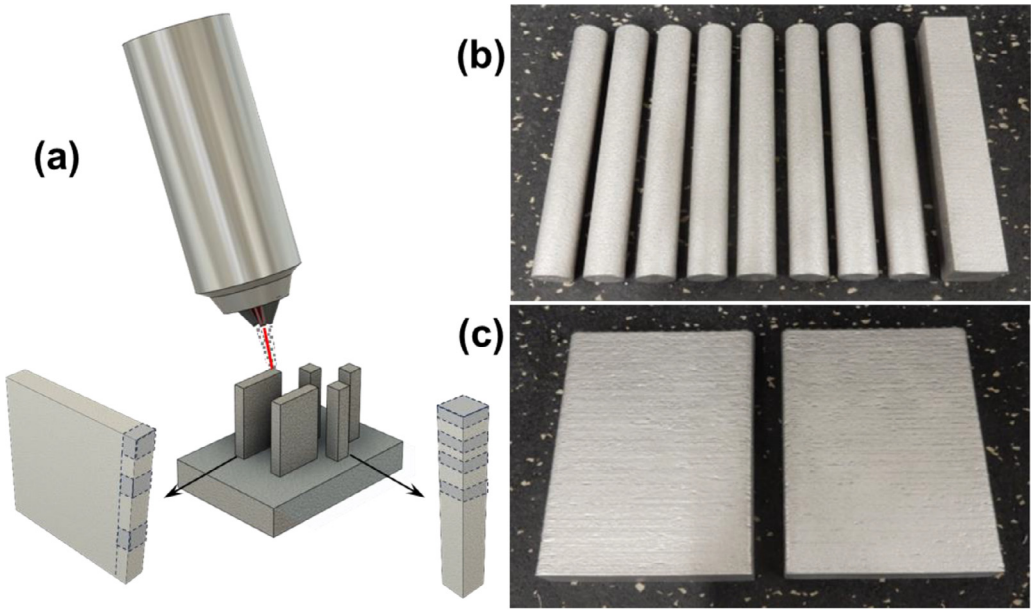

d	Laser Power (W)	Powder Feed Rate (g/min)	Travel Speed (mm/s)
Bars	350	15.0	1016
	750	11.0	1016
	1070	16.3	1016
Blocks	2000	18.6	1016
	2620	27.0	762

Fig. 2. A Schematic illustration of the NASA HR-1 bars and blocks deposited via LP-DED with a coaxial laser-powder system, (b) cylindrical and rectangular bars with a length of 114 mm and diameter/thickness of 17 mm, and (c) 114×114×17 mm^3 blocks deposited with the process parameters reported in (d).

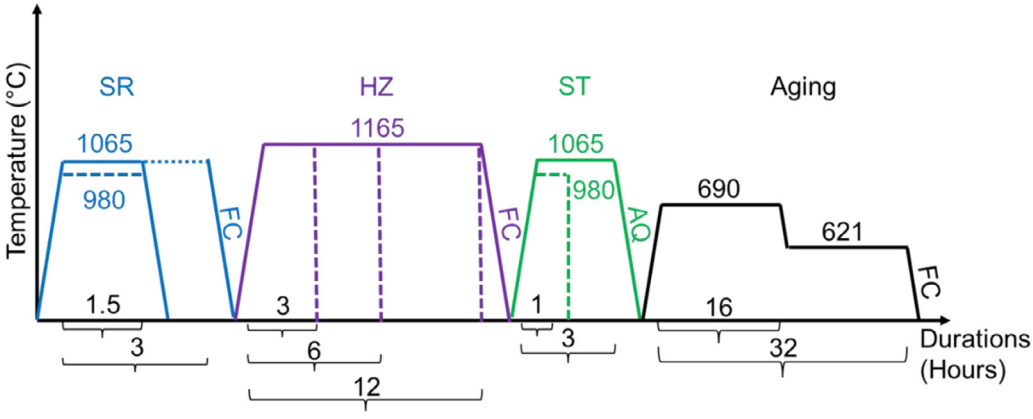

Fig. 3. The HT cycle for NASA HR-1 consisting of SR, HZ, ST, and Aging.

and blocks were heat-treated and machined into the geometry of tensile specimens according to ASTM E8 [15] (see Fig. S1 in the Supplemental Material). Tensile tests were conducted at a strain rate of 0.005 mm/mm/min up until yielding and continued until fracture with a strain rate of 0.05 mm/mm/min. The percent elongation to failure, ultimate tensile strength (UTS), and the 0.2% offset yield strength (YS) were calculated. Lastly, fracture surfaces of select specimens were examined using a Zeiss Crossbeam 550 SEM.

Experimental results and discussion

Laser penetration depth

The melt pool depth, overlap depth, and width were measured for different laser power in NHT samples. As shown in Fig. 4 and Fig. 5(a), the melt pool size increased with increasing the laser power and spot size as expected [8].

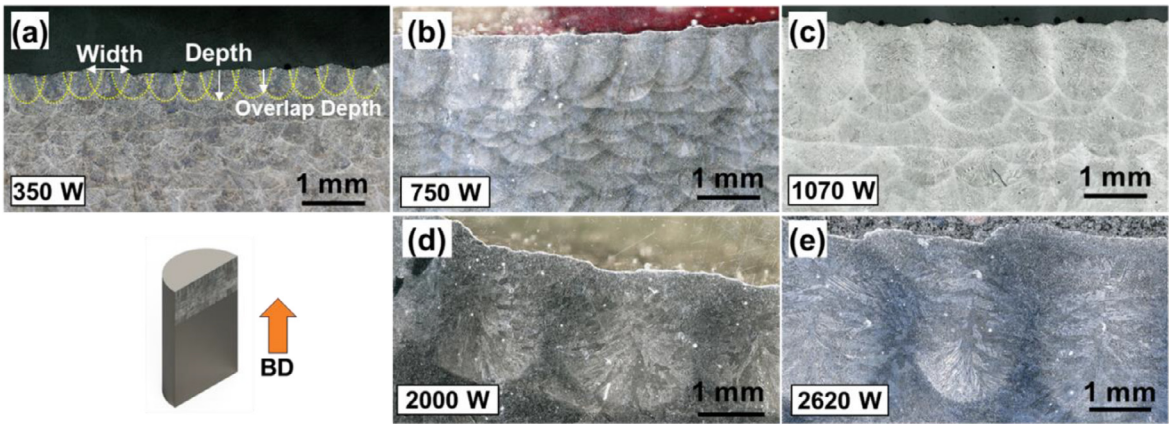

Fig. 4. NASA HR-1 melt pool morphologies along the BD for (a) 350, (b) 750, (c) 1070, (d) 2000, and (e) 2620 W laser power.

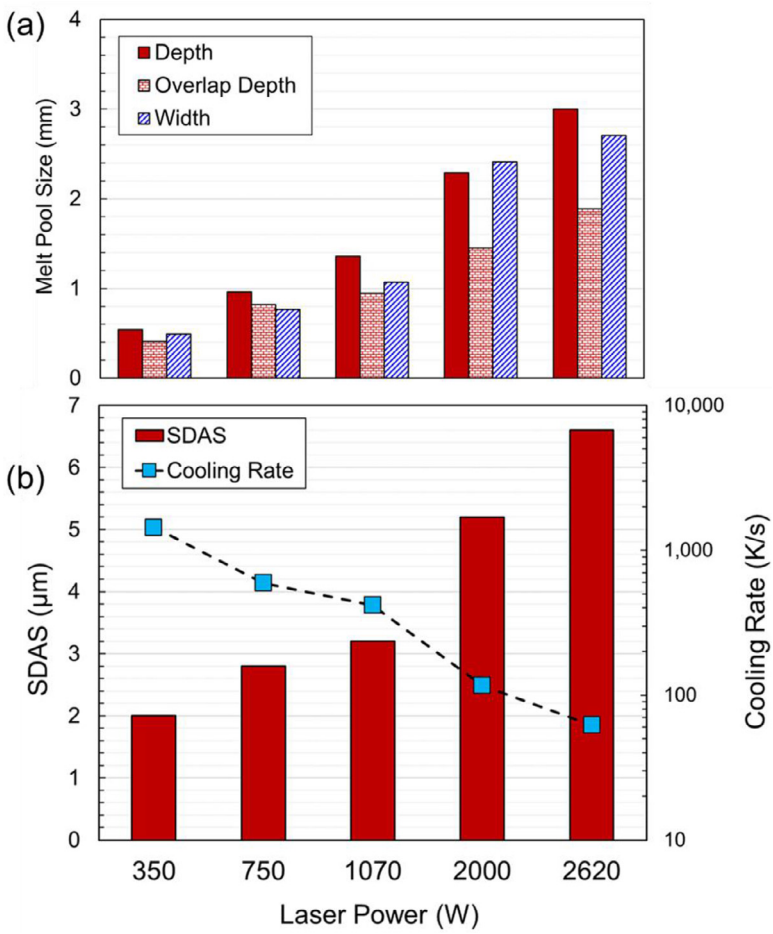

Fig. 5. (a) Experimentally measured melt pool depth, overlap depth, and width, and (b) experimentally measured SDAS, and calculated cooling rate.

Moreover, the secondary dendrite arm spacing (SDAS) was obtained experimentally in the NHT etched specimens for each condition by dividing the lengths of observable primary dendrites by the numbers of secondary arms on the primary dendrites and taking the average (see Fig. S2 in the Supplemental Material). The results are presented in Fig. 5(b). Material strength, hardness, and HT time to diminish alloy segregation and interdendritic detrimental phases are known to be influenced by the SDAS [16]. As NASA HR-1 is an austenitic iron-based superalloy and has a similar chemical composition to that of the A286, the cooling rate during HR-1 deposition was estimated using the SDAS-cooling rate equation of A286 proposed in Ref. [16]:

$$SDAS = K\left(\frac{dT}{dt}\right)^{n} \quad (1)$$

where K and n are material-dependent constants and are usually obtained empirically. Frisk et al. [16] reported 31.7 and −0.38 for K and n, respectively. The calculated cooling rates are presented in Fig. 5(b). As shown, increasing laser power resulted in slower cooling rates, consistent with the results in Ref. [8,17].

Defect-/micro-structure

Porosity was evaluated on the longitudinal plane (along the BD) for different laser power in the NHT condition. As seen in Fig. 6(a), the defect area fractions were relatively low for all conditions, resulting in material densities higher than 99.70%. It was also noted that the laser power of 750 W could result in the lowest defect area fraction among

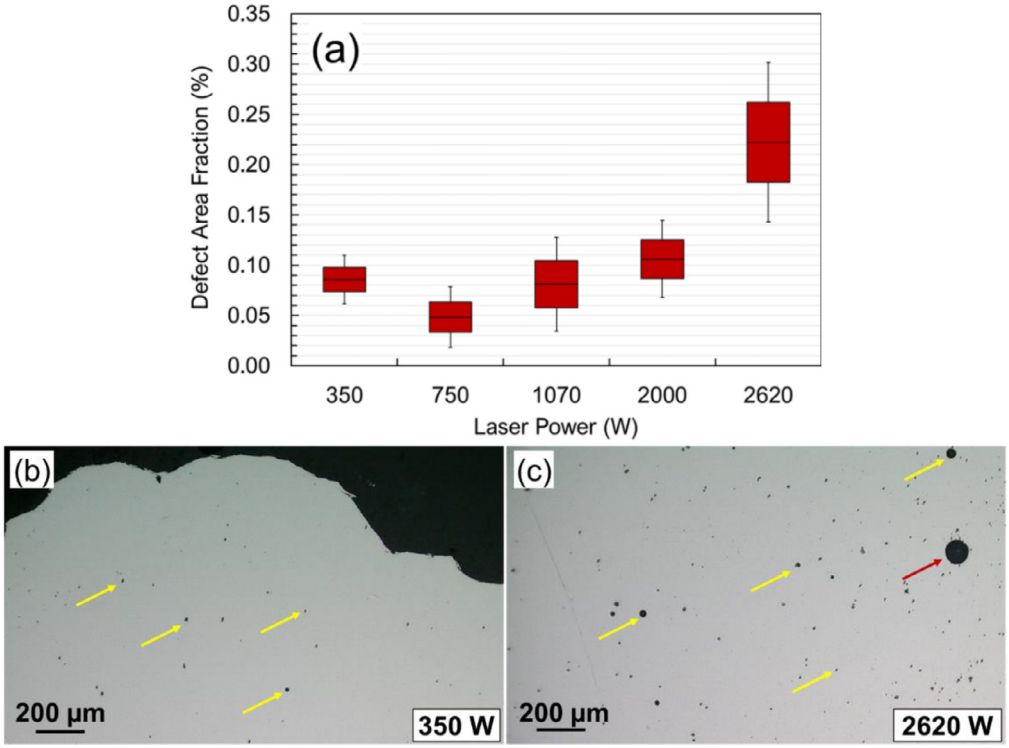

Fig. 6. (a) 2D porosity, in percent area fraction, for different laser power in the NHT condition and polished cross-sections of the specimens deposited via (b) 350 W and (c) 2620 W laser power. Yellow and red arrows show the small and large gas-entrapped pores, respectively.

all laser power examined. Most defects were gas-entrapped pores (see Fig. 5(b)), which are common defects in LP-DED, typically due to localized vaporization, feedstock porosity, or the shielding gas entrapment [17]. As the laser power was increased to 2620 W, some large spherical pores (~105 µm) were also noted. In addition, the number of defects considerably increased for the 2620 W laser power, most likely due to the easier entrapment of processing shielding gas in the deeper melt pools.

Microstructure changes with varying laser power and HT steps were investigated. Although the microstructure was examined for each laser power, only the ones corresponding to 750 W are reported in this manuscript, and the remainders are provided in the Supplemental Material. In addition, the overall changes in low angle grain boundary (LAGB), annealing twin boundary (Σ3), and grain size (ξ) were traced with different HT steps and reported in Table 2. As seen in Fig. 7(a) and Fig. S8 in the Supplemental Material, the microstructure in the NHT condition consisted of some equiaxed grains, mainly near the melt pool boundaries and columnar grains due to the primary heat dissipation trajectory along the BD [18,19]. Similar microstructures were noted with varying laser power (see Figs. S3(a), S4(a), S5(a), and S6(a) in the Supplemental Material).

After SR1065/1.5, the microstructure recrystallized, and some equiaxed grains were noted. However, it is reported in Ref. [4] that an SR cycle alone cannot eliminate the dendritic microstructure, and a subsequent hot isostatic pressing or HZ is required. The HZ cycle provided a homogeneous microstructure (see Fig. 7(c)). In this condition, the Σ3 increased from 1% in the NHT condition to 66% after HZ, and ξ increased by ~3.5 times. After ST (see Fig. 7(d) and Table 2), the fractions of Σ3 and LAGBs were somewhat similar to the HZ condition. In addition, ξ increased with ST by ~ 23 µm.

Lastly, the microstructure was evaluated after aging (see Fig. 7(e) and Table 2). The LAGBs were at their minimum, representing the decrease in dislocation density and complete recrystallization, while the Σ3 remained almost constant. As seen in Fig. 8 and Fig. S9 in the Supplemental Material, nanometer-sized γ' precipitates (bright spot-like features, with some of them indicated by yellow arrows) were abundant after aging, which were uniformly distributed within the grains.

Table 2
A summary of LAGB, Σ3, and ξ at different stages of HT for LP-DED NASA HR-1 deposited under different laser power.

HT	NHT	SR1065/1.5	HZ1165/12	ST980/1	Aged
Laser Power: 350 W					
LAGB (%)	12	2	1	2	7
Σ3 (%)	1	62	69	60	51
ξ (µm)	24	63	53	51	61
Laser Power: 750 W					
LAGB (%)	12	1	1	2	2
Σ3 (%)	1	62	66	66	65
ξ (µm)	22	82	76	99	146
Laser Power: 1070 W					
LAGB (%)	17	11	1	2	1
Σ3 (%)	2	2	71	65	63
ξ (µm)	31	33	103	75	143
Laser Power: 2000 W					
LAGB (%)	13	2	2	3	2
Σ3 (%)	1	65	66	75	70
ξ (µm)	40	142	29	71	95
Laser Power: 2620 W					
LAGB (%)	9	6	1	6	2
Σ3 (%)	2	33	65	69	64
ξ (µm)	62	46	76	133	113

Therefore, it may be assumed that the material strength increases in the aged condition due to the increased volume fraction of γ' precipitates [1] which can act as dislocation pinners. Ascribing the material strength increase to γ' but not the other known precipitates type, i.e., η, was also due to latter having a distinct needle-like morphology which could be easily detected if present.

The segregation of major alloying elements (i.e., Ti) was investigated for all NHT samples (see Fig. S10 in the Supplemental Material) and HT conditions for the 750 W (see Fig. 9). As shown in the NHT condition in Fig. 9(a), there was clear segregation of Ti, which fluctuates between 2 and 8%. As previously mentioned, limited Ti is generally added to the alloy to enhance the material strength by increasing the γ' volume fraction. After deposition via LP-DED, the microstructure is typically dendritic, due to the high cooling rates, with the primary dendrite arts

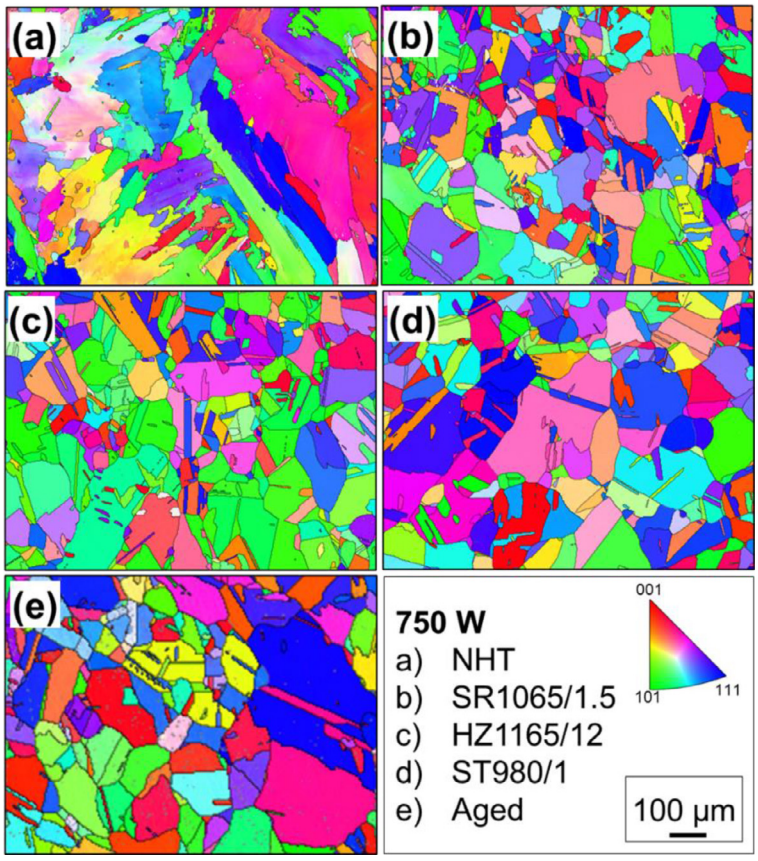

Fig. 7. (a–e) Microstructure of the LP-DED NASA HR-1 parts deposited via 750 W laser power in different HT conditions.

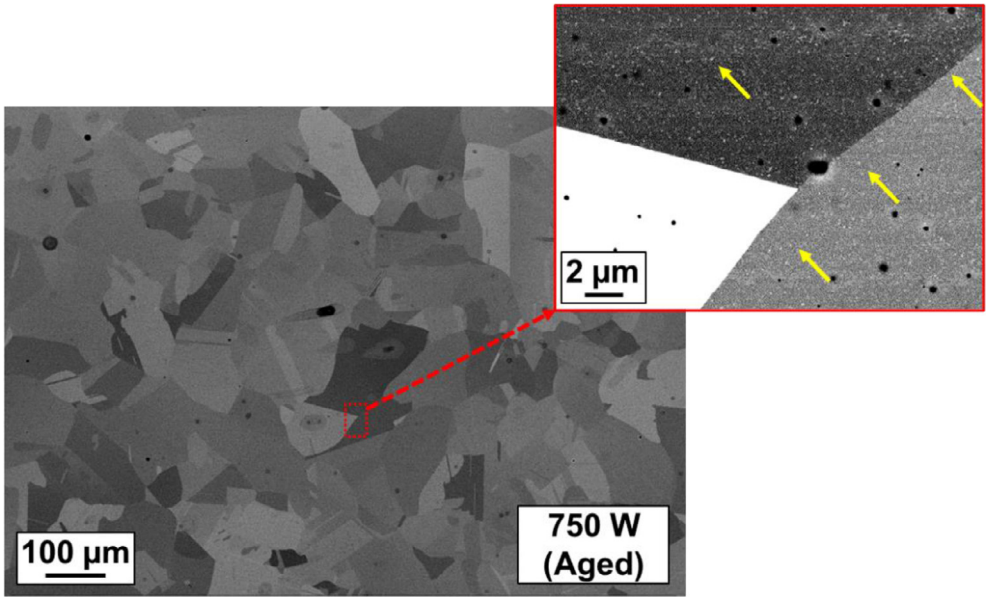

Fig. 8. ECCI images of the 750 W specimen in the SR1065/1.5-HZ1165/6-ST1065/1-Aged690–620/16–16 conditions. The yellow arrows indicate the γ' precipitates.

oriented toward the melt pool center and aligned with the temperature gradients [20]. The rapid solidification process limits mass diffusion, which results in the dendrites having a "cored" composition characteristic with the centers of dendrites being Ni rich and the interdendritic regions being Ti rich [20].

The Ti segregation has been reported as a major challenge in LP-DED NASA HR-1 which can promote the formation of η-phase (Ni_3Ti) precipitates at grain boundaries and consequently reduce material ductility and HEE resistance [1,4,20]. Upon SR1065/1.5, only minor Ti segregation was observed in Fig. 9(b). The degree of elemental segregation was greatly reduced when the specimens were homogenized, i.e., HZ1165/3–12 (see Fig. 9(c)–(e)). The reduced Ti segregation after SR has been associated with its dissolution effects on the dendritic microstructures [20]. However, there is still a possibility of Ti segregation along the grain boundaries if the dissolution is not complete before recrystallization and grain growth [20]. This was observed in some spots after HZ1165/3 (see Fig. 9(c)). In addition, the ST temperature of 1065 °C was effective in dissolving Ti, as no noticeable segregation was

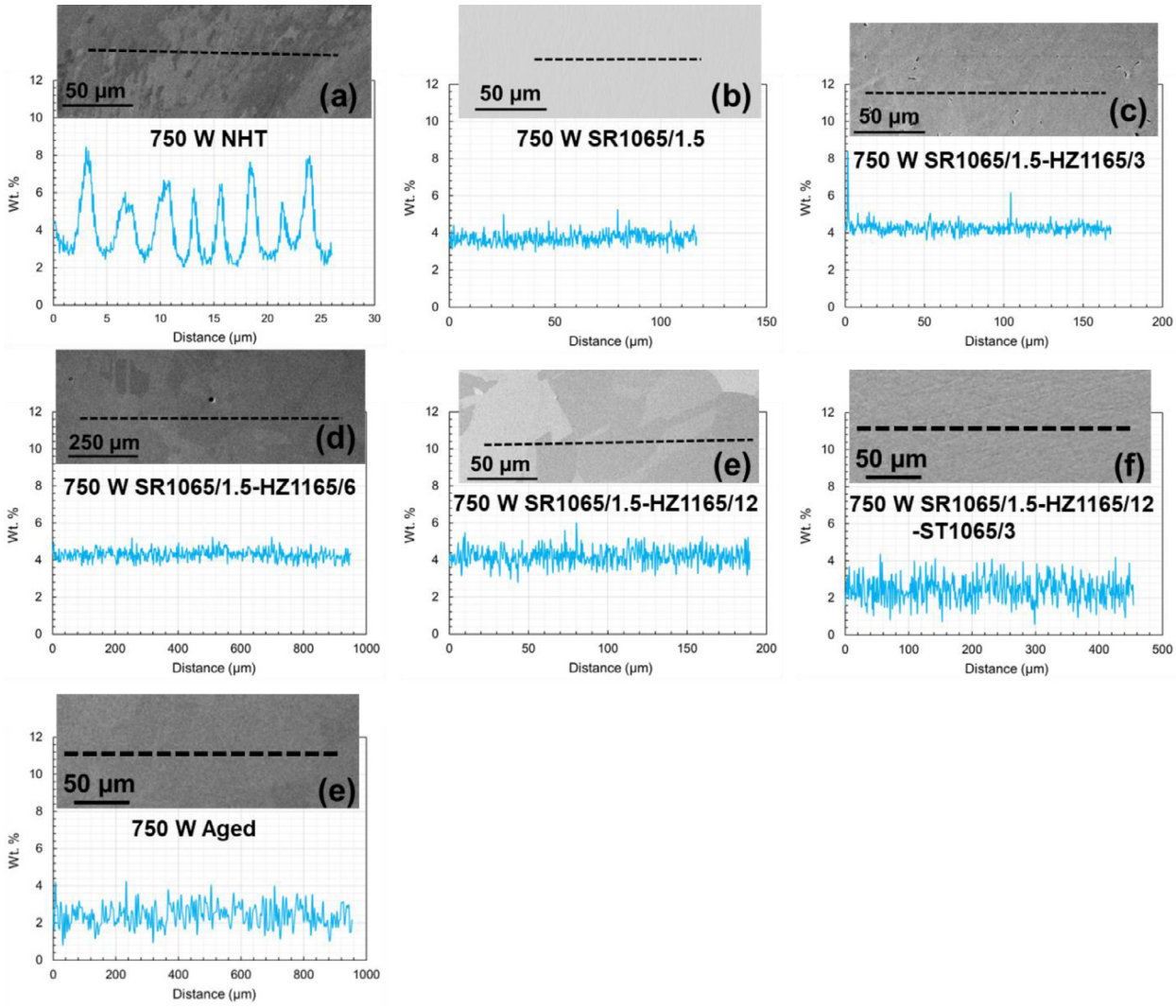

Fig. 9. Ti concentrations in line scans performed on the LP-DED NASA HR-1 750 W specimen in (a) NHT, (b) SR1065/1.5, (c) SR1065/1.5-HZ1165/3, (d) SR1065/1.5-HZ1165/6, (e) SR1065/1.5-HZ1165/12, (f) SR1065/1.5-HZ1165/12-ST1065/3, and (e) SR1065/1.5-HZ1165/6-ST1065/1-Aged690–620/16–16 conditions.

observed after conducting the ST1065/3 and two-step aging, which was consistent with the results in Ref. [1,20]. The proposed HT effectively reduced the Ti segregation for all laser power, induced significant recrystallization and grain growth, and diminished material anisotropy. It needs to be mentioned that Ti segregation is reported to be absent in the wrought and cast NASA HR-1 microstructures, as the fabrication processes permitted more time for Ti to diffuse uniformly in the microstructure [20]. Overall, the HT resulted in similar microstructures among all fabrication conditions although the average grain size was somewhat smaller in the case of 350 W laser power than others.

Rockwell B hardness (HRB)

HRB of the NASA HR-1 samples was evaluated for all the HT conditions to ensure the proposed HT is suitable for LP-DED NASA HR-1. As seen in Fig. 10 and Table 3, HRB changes with altering laser power in the NHT condition were negligible. All SR cycles, regardless of temperature, considerably increased the HRB, which might be attributed to the presence of γ' and η precipitates during the furnace cooling and material recovery after SR [1], although other strengthening mechanisms may be also involved. It needs to be stated that prolonged exposure at certain elevated temperatures, such as during the furnace cooling after SR, can encourage the nucleation of γ' and η precipitates [3,21]. Such features have been also commonly seen in many other Ni-base superalloys, such as Haynes 282 [22].

Although they can achieve high strength, the η precipitates reduce ductility and need to be removed via further annealing steps. Increasing the SR temperature from 980 °C to 1065 °C did not affect the HRB, which further confirmed this speculation. However, the higher SR temperature did result in partial recrystallization in NASA HR-1 [4] (see Fig. S7(a) & (b) in the Supplemental Material). Increasing the SR time from 1.5 to 3 h seemed unnecessary as it did not affect the HRB nor the microstructure (see Fig. S7(c) in the Supplemental Material). In the HZ condition, the HRB was considerably reduced, consistent with Ref. [1]. The significant drop in hardness after HZ was primarily due to the dissolution of any precipitates, although microstructure homogenization and recrystallization, shown in Fig. 7(c) & (d), could have also contributed.

In addition, it was noted that the HRB changes between different HZ durations (i.e., 3, 6, and 12 h) were negligible (see Fig. 10). However, a minimum duration of 6 h was selected for HZ1165 as some studies still reported Ti segregation with HZ1165/3 [4]. A subsequent ST was conducted on the homogenized specimens. The ST can prepare the material for the last precipitation hardening (i.e., aging) step by taking it back above its solution temperature and cooling rapidly to ambient

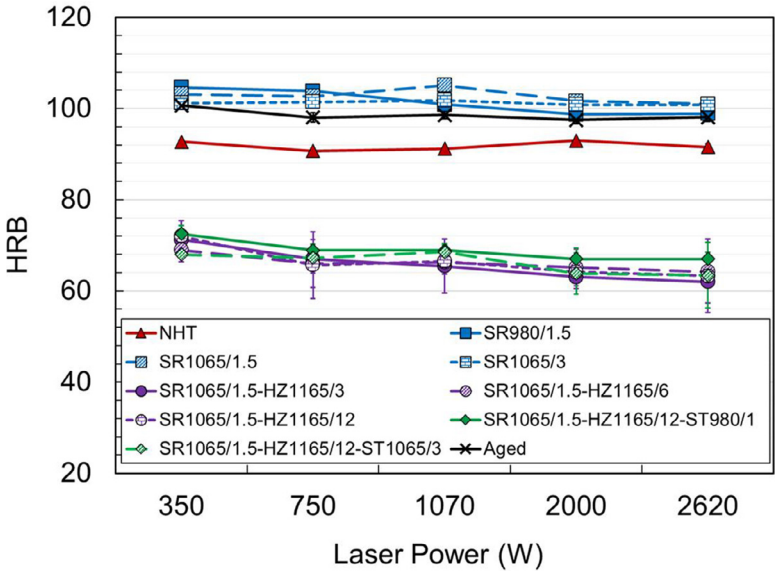

Fig. 10. HRB values for LP-DED NASA HR-1 for different HTs and laser power.

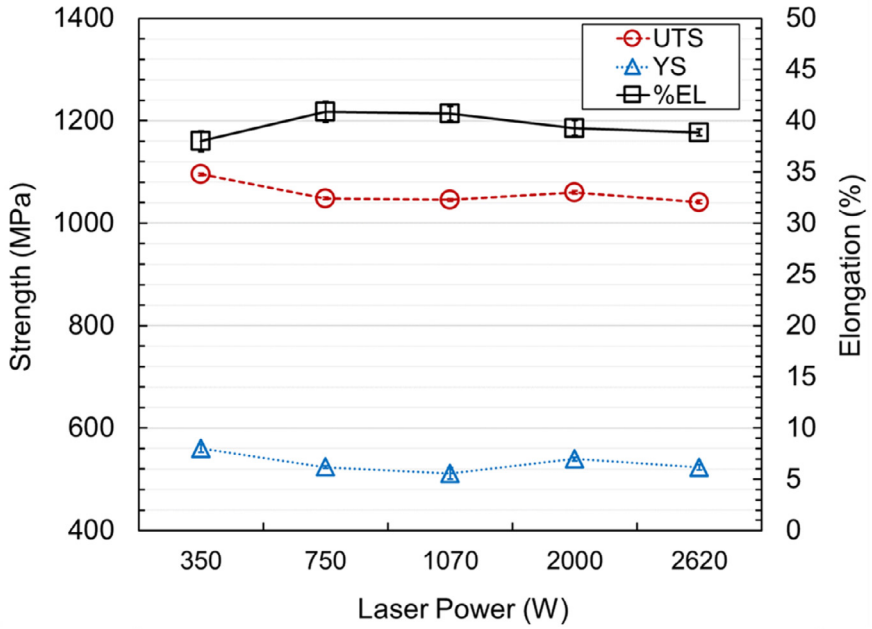

Tensile Property	Laser Power (W)					Wrought
	350	750	1070	2000	2620	
UTS (MPa)	1096 ± 3	1049 ± 3	1045 ± 3	1060 ± 3	1042 ± 3	1260
YS (MPa)	561 ± 8	524 ± 3	511 ± 11	540 ± 4	523 ± 5	944
%EL	38 ± 1	41 ± 1	41 ± 1	39 ± 1	39 ± 0	24

Fig. 11. Tensile properties of LP-DED NASA HR-1 specimens in the aged condition, fabricated by different laser power and compared with the wrought NASA HR-1 [3].

temperature by argon or water quench to maintain the η-phase free, super-saturated solid solution [1]. As seen in Fig. 10, the ST did not increase the material hardness, which was consistent with the minimal microstructural changes due to ST, as observed in Fig. 7(c) & (d). In both HZ and ST conditions, the changes in HRB with varying laser power were also negligible.

Although minor changes were noted with ST at 980 and 1065 °C, the latter was used for the final ST since the formation of η precipitates was reported in Ref. [1] by conducting aging after ST980. Due to minor variations with time, the specimens were kept for only 1 h during ST1065. A two-step aging at 690 and 620 °C with a total of 32 h was conducted to enhance the material hardness. As evident in Fig. 10, the HRB in the aged condition was considerably higher than in the NHT condition, even though the ξ increased. This increase in HRB was attributed to the effects of two-step aging at high and low temperatures, promoting the formation of primary γ' and finer secondary or tertiary γ'

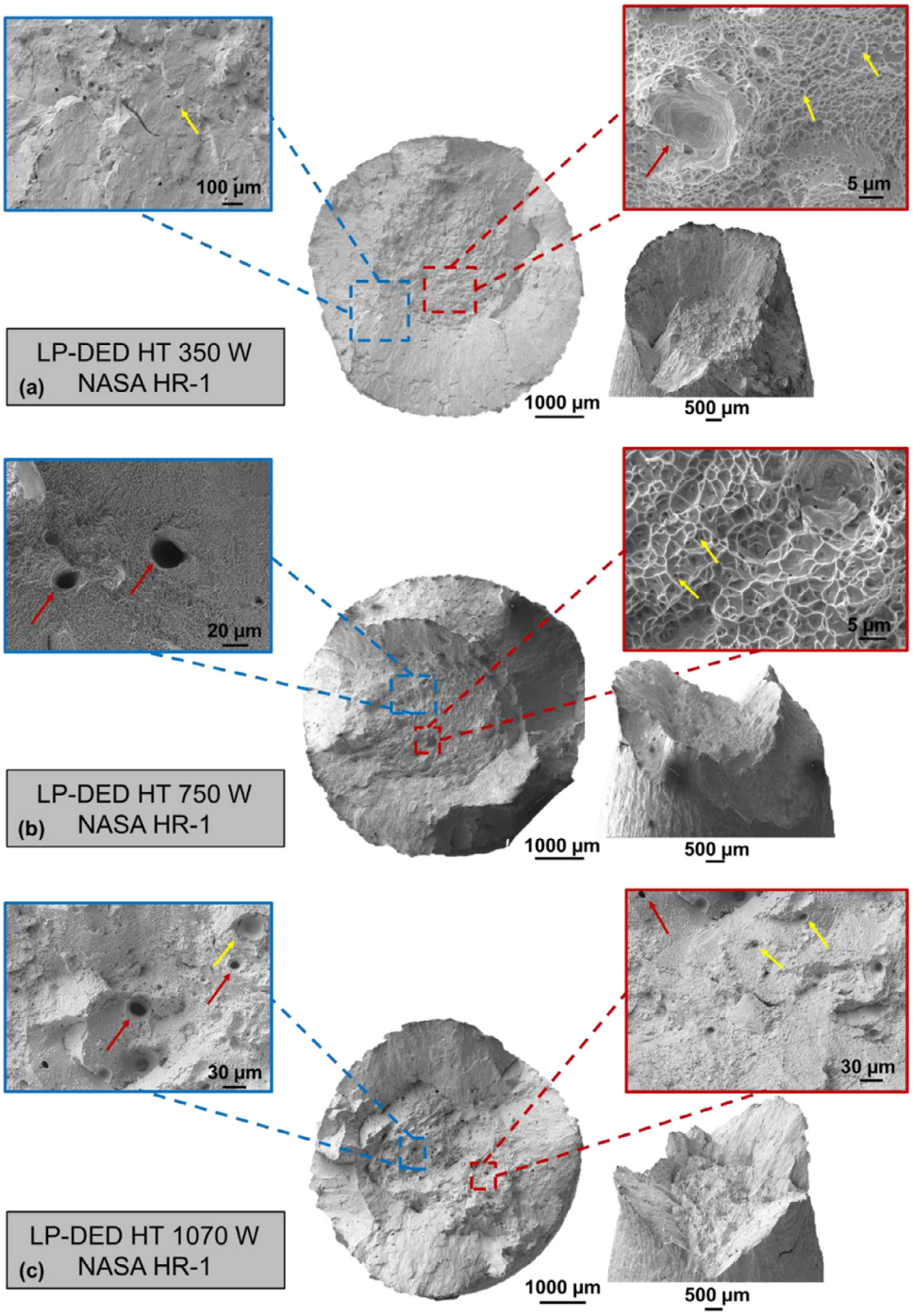

Fig. 12. Fracture surfaces of the LP-DED NASA HR-1 specimens deposited with (a) 350, (b) 750, (c) 1070, (d) 2000, and (e) 2620 W laser power in the aged condition.

Table 3
A summary of HRB values for LP-DED NASA HR-1 samples in different HT conditions and deposited using different laser powers.

Laser Power (W) →	350	750	1070	2000	2620
NHT	93 ± 0	91 ± 1	91 ± 0	93 ± 0	92 ± 1
SR980/1.5	105 ± 0	104 ± 1	101 ± 0	99 ± 0	99 ± 1
SR1065/1.5	103 ± 0	103 ± 1	105 ± 0	102 ± 1	101 ± 1
SR1065/3	101 ± 1	101 ± 1	102 ± 2	101 ± 1	101 ± 1
SR1065/1.5-HZ1165/3	71 ± 2	67 ± 3	65 ± 6	63 ± 2	62 ± 5
SR1065/1.5-HZ1165/6	69 ± 3	66 ± 5	66 ± 2	65 ± 4	64 ± 3
SR1065/1.5-HZ1165/12	72 ± 3	66 ± 7	66 ± 3	64 ± 4	63 ± 8
SR1065/1.5-HZ1165/12-ST980/1	72 ± 2	69 ± 1	69 ± 2	67 ± 2	67 ± 1
SR1065/1.5-HZ1165/12-ST1065/3	68 ± 0	67 ± 2	69 ± 1	64 ± 5	63 ± 7
Aged	101 ± 1	98 ± 1	99 ± 1	98 ± 1	98 ± 1

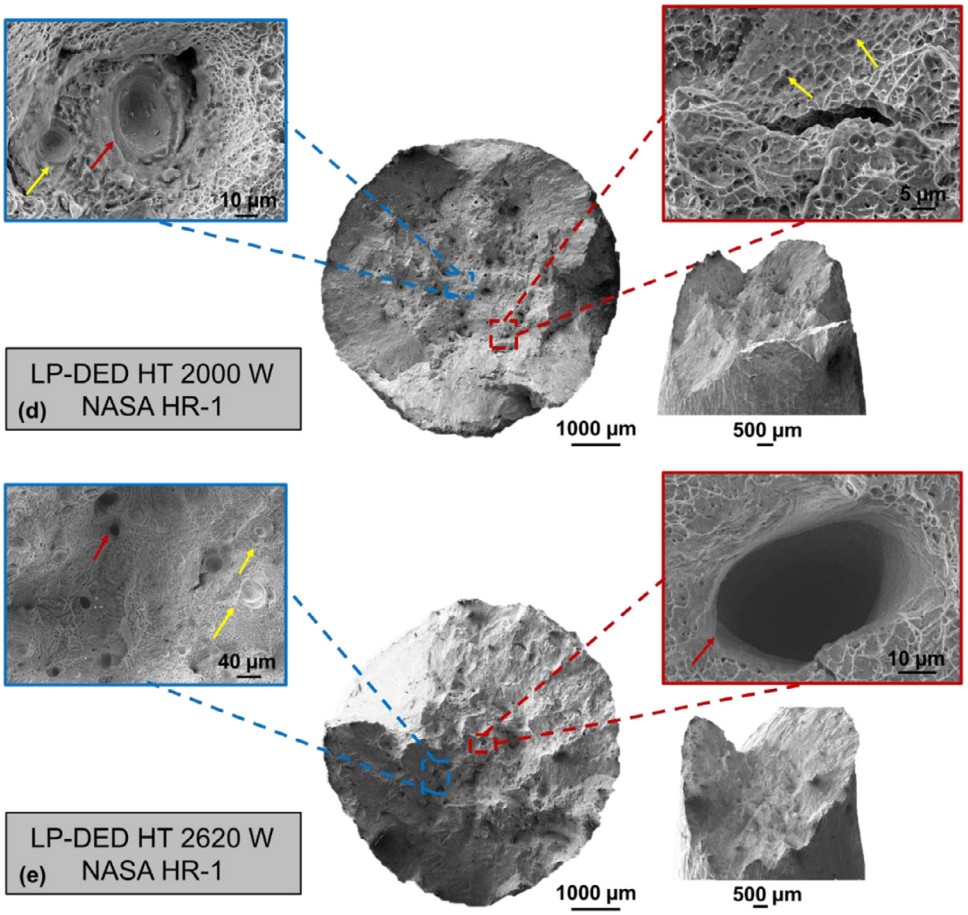

precipitations in the material [1], as seen in Fig. 8. The HRB in the aged condition was, however, slightly lower than in the SR condition, which can be due to presence of both γ' and η in the material after SR [1].

Tensile properties

Tensile properties are shown in Fig. 11. Although not significant, the specimens deposited with 350 W laser power illustrated the highest UTS and YS among all conditions, and the remainders were somewhat comparable. This behavior was attributed to the smaller grains in the 350 W specimens [23,24] after aging (see Table 2) due to higher cooling rates during deposition [19]. The variations in ductility (represented by% Elongation in Fig. 11) were negligible (< 3%), even though the defect content was somewhat different (see Fig. 6). Indeed, it has been indicated that the ductility of the AM materials is not significantly affected unless the porosity is ~5% or higher [25]. Therefore, it can be assumed that the higher defect content of the specimen deposited at 2620 W (relative density of 99.7%) was not as critical in influencing the material ductility [26]. In Fig. 11, tensile properties of wrought NASA HR-1, which is typically hot- or cold-rolled, are also reported [3]. As seen, the wrought material has higher UTS and YS, while exhibiting lower ductility than the LP-DED specimens.

Fracture surfaces of select specimens deposited with various laser power were investigated. Dimples and the classical cup-and-cone feature were present on fracture surfaces of all specimens (illustrated by yellow arrows in Fig. 12), indicating the ductile fracture mechanism. Large gas-entrapped pores (illustrated by red arrows in all figures) were frequently observed on the fracture surface as the laser power was increased. It seemed that in all specimens, the dominating failure mechanism was the coalescence of microvoids resulting in the fracture, even though the gas-entrapped pores could have contributed to the nucleation of fracture. This was consistent with the observation that the ductility did not significantly vary with increasing laser power. In addition, the material exhibited a considerable hardening while testing (see Table S1 in the Supplemental Material), which was attributed to the lower dislocation density after aging, the relatively good ductility, and the fairly large grain size. Tensile behavior was obtained for specimens fabricated with all laser power and illustrated in Fig. S11 in the Supplemental Material.

Conclusions

In this study, LP-DED NASA HR-1 alloy specimens were deposited using various laser power to assess their effect on defect-/micro-structure and mechanical properties. In addition, the effect of different heat treatments on the microstructure was investigated. The following conclusions can be drawn based on the experimental results:

Increasing the laser power and associated laser spot size increased the melt pool depth, overlap depth, and width while decreasing the cooling rate.

A heat treatment schedule consisting of stress relief at 1065 °C for 1.5 h, homogenization at 1165 °C for 6 h, solution treatment at 1065 °C for 1 h, and two-step aging at 690 °C and 620 °C with a total of 32 h was effective to increase the strength in NASA HR-1. This heat treatment efficiently recrystallized and homogenized the microstructure and compensated for the loss in material strength by the formation of γ' precipitates.

Ti segregation was evident in the non-heat-treated condition across the dendrites for all laser powers, which was diminished as the material underwent the complete heat treatment cycle.

A slightly higher ultimate tensile and yield strength were observed for the parts deposited using lower laser power due to the higher cooling

rates, forming finer grains. Ductility, however, did not change with laser power.

Practical component manufacturing using additive manufacturing must properly balance the required material properties with process economics. Increasing spot size and laser power can substantially reduce the overall build time but at a detriment to the feature size. Each component should be evaluated based on various metrics, including feature resolution needed, microstructure, and material property requirements, in addition to economics such as build cost and schedule. This study provided an initial baseline to aid designers with variations of the laser power to understand potential impacts on the NASA HR-1 alloy microstructure and typical mechanical properties at room temperature.

Declaration of Competing Interest

The authors declare that they have no known competing financial interests or personal relationships that could have appeared to influence the work reported in this paper.

Data Availability

Data will be made available on request.

Acknowledgments

This paper is based upon the work partially funded by the National Aeronautics and Space Administration (NASA) under Award #80MSFC19C0010. Any subjective views or opinions that might be expressed in the paper do not necessarily represent the views of NASA or the United States Government.

Supplementary materials

Supplementary material associated with this article can be found, in the online version, at doi:10.1016/j.addlet.2022.100097.

References

[1] C. Katsarelis, P. Chen, P. Gradl, C. Protz, Z. Jones, D. Ellis, L. Evans, Additive manufacturing of NASA HR-1 material for liquid rocket engine component applications, M19-7797, JANNAF (2019).
[2] P.R. Gradl, C.S. Protz, Technology advancements for channel wall nozzle manufacturing in liquid rocket engines, Acta Astronaut. 174 (2020) 148–158, doi:10.1016/j.actaastro.2020.04.067.
[3] P. Chen, M. Mitchell, Alloy NASA-HR-1, Aerosp. Struct. Met. Handb. (2005) https://ntrs.nasa.gov/citations/20050182936.
[4] P.R. Gradl, T.W. Teasley, C.S. Protz, C. Katsarelis, P. Chen, Process development and hot-fire testing of additively manufactured NASA HR-1 for liquid rocket engine applications, in: AIAA Propuls. Energy 2021 Forum, American Institute of Aeronautics and Astronautics, Reston, Virginia, 2021, pp. 1–23, doi:10.2514/6.2021-3236.
[5] A. Birken, D. Noel, Metallurgical and thermal processing investigation of additively manufactured superalloys JBK-75 and NASA-HR-1 (2021).
[6] P.R. Gradl, A. Cervone, E. Gill, Surface texture characterization for thin-wall NASA HR-1 Fe–Ni–Cr alloy using laser powder directed energy deposition (LP-DED), Adv. Ind. Manuf. Eng. 4 (2022) 100084, doi:10.1016/j.aime.2022.100084.
[7] R.P. Mudge, N.R. Wald, Laser engineered net shaping advances additive manufacturing and repair, Welding Journal 86 (2007) 44–48.
[8] A. Soltani-Tehrani, R. Shrestha, N. Phan, M. Seifi, N. Shamsaei, Establishing specimen property to part performance relationships for laser beam powder bed fusion additive manufacturing, Int. J. Fatigue 151 (2021) 106384, doi:10.1016/j.ijfatigue.2021.106384.
[9] R. Shrestha, N. Shamsaei, M. Seifi, N. Phan, An investigation into specimen property to part performance relationships for laser beam powder bed fusion additive manufacturing, Addit. Manuf. 29 (2019) 100807, doi:10.1016/j.addma.2019.100807.
[10] N. Shamsaei, A. Yadollahi, L. Bian, S.M. Thompson, An overview of direct laser deposition for additive manufacturing; Part II: mechanical behavior, process parameter optimization and control, Addit. Manuf. 8 (2015) 12–35, doi:10.1016/j.addma.2015.07.002.
[11] A. Yadollahi, N. Shamsaei, Additive manufacturing of fatigue resistant materials: challenges and opportunities, Int. J. Fatigue 98 (2017) 14–31, doi:10.1016/j.ijfatigue.2017.01.001.
[12] ASTM E2546-15Standard practice for instrumented indentation testing, ASTM International, West Conshohocken, PA, 2018.
[13] ASTM E407-07Standard practice for microetching metals and alloys, ASTM International, West Conshohocken, PA, 2015.
[14] NASA MSFC-SPEC-3717 - Specification for control and qualification of laser powder bed fusion metallurgical processes, (2017).
[15] ASTM E8/E8M-22Standard test methods for tension testing of metallic materials, ASTM International, West Conshohocken, PA, 2022.
[16] R. Frisk, N.Å.I. Andersson, B. Rogberg, Cast structure in alloy A286, an iron-nickel based superalloy, Metals 9 (2019), doi:10.3390/met9060711.
[17] D. Svetlizky, M. Das, B. Zheng, A.L. Vyatskikh, S. Bose, A. Bandyopadhyay, J.M. Schoenung, E.J. Lavernia, N. Eliaz, Directed energy deposition (DED) additive manufacturing: physical characteristics, defects, challenges and applications, Mater. Today 49 (2021) 271–295, doi:10.1016/j.mattod.2021.03.020.
[18] P.D. Nezhadfar, A.S. Johnson, N. Shamsaei, Fatigue behavior and microstructural evolution of additively manufactured inconel 718 under cyclic loading at elevated temperature, Int. J. Fatigue (2020) 105598, doi:10.1016/j.ijfatigue.2020.105598.
[19] A. Yadollahi, N. Shamsaei, S.M. Thompson, D.W. Seely, Effects of process time interval and heat treatment on the mechanical and microstructural properties of direct laser deposited 316L stainless steel, Mater. Sci. Eng. A 644 (2015) 171–183, doi:10.1016/j.msea.2015.07.056.
[20] P.S. Chen, C.C. Katsarelis, W.M. Medders, P.R. Gradl, Segregation evolution and diffusion of titanium in directed energy deposited NASA HR-1, No. NASA/TM-20210013649, (2021).
[21] P.S. Chen, B. Panda, B.N. Bhat, NASA-HR-1, a new hydrogen-resistant Fe-Ni-base superalloy, Hydrog. Eff. Mater. (1996) 1011–1019, doi:10.1002/9781118803363.ch89.
[22] R. Ghiaasiaan, N. Ahmad, P.R. Gradl, S. Shao, N. Shamsaei, Additively manufactured haynes 282: effect of unimodal vs. bimodal γ'- microstructure on mechanical properties, Mater. Sci. Eng. A 831 (2022) 142234, doi:10.1016/j.msea.2021.142234.
[23] E.O. Hall, The deformation and ageing of mild steel: III discussion of results, Proc. Phys. Soc. Sect. B 64 (1951) 747–753, doi:10.1088/0370-1301/64/9/303.
[24] N.J. Petch, The cleavage strength of polycrystals, J. Iron Steel Inst. 174 (1953) 25–28.
[25] A. Mostafaei, C. Zhao, Y. He, S. Reza Ghiaasiaan, B. Shi, S. Shao, N. Shamsaei, Z. Wu, N. Kouraytem, T. Sun, J. Pauza, J.V. Gordon, B. Webler, N.D. Parab, M. Asherloo, Q. Guo, L. Chen, A.D. Rollett, Defects and anomalies in powder bed fusion metal additive manufacturing, Curr. Opin. Solid State Mater. Sci. 26 (2022) 100974, doi:10.1016/j.cossms.2021.100974.
[26] A. du Plessis, I. Yadroitsava, I. Yadroitsev, Effects of defects on mechanical properties in metal additive manufacturing: a review focusing on X-ray tomography insights, Mater. Des. 187 (2020) 108385, doi:10.1016/j.matdes.2019.108385.